Journal of Marine Research, 59, 167–191, 2001

Journal of
MARINE RESEARCH

Volume 59, Number 2

North Pacific internal tides from the Aleutian Ridge: Altimeter observations and modeling

by Patrick F. Cummins[1], Josef Y. Cherniawsky[1] and Michael G. G. Foreman[1]

ABSTRACT

Internal tides radiating into the North Pacific from the Aleutian Ridge near Amukta Pass are examined using 7 years of Topex/Poseidon altimeter data. The observations show coherent southward phase propagation at the M_2 frequency over a distance of at least 1100 km into the central Pacific. Barotropic and baroclinic models are applied to study this internal tidal signal. Results from the barotropic model show that the strongest cross-slope volume and energy fluxes occur in the vicinity of Amukta Pass, helping to establish this region as an important site for baroclinic energy conversion along the eastern half of the ridge.

A two-dimensional version of the Princeton Ocean Model is used to simulate internal tide generation and propagation. A comparison between the altimeter data south of the ridge and the sea-surface signature of the internal tide signal of the model shows good agreement for the phase, both close to the source and well into the far field. Comparison of the phase between model and data also provides evidence for wave refraction. This occurs due to the slow modulation of wavelength associated with the variation in the Coriolis parameter encountered as the internal tide propagates southward. The model results suggest that the net rate of conversion of barotropic to baroclinic energy is about 1.8 GW in the vicinity of Amukta Pass. This represents about 6% of the local barotropic energy flux across the ridge and perhaps 1% of global baroclinic conversion.

1. Introduction

Prior to the launch of the Topex-Poseidon (T/P) mission in August, 1992, it was widely held that oceanic internal tides generally did not propagate more than short distance away from a source region before becoming ‘incoherent,’ that is, before losing their phase relation with the generating surface tide. For example, in observations from moored

1. Institute of Ocean Sciences, Sidney, BC, Canada V8L 4B2. ***email: cumminsp@pac.dfo-mpo.gc.ca***

sensors, internal tides often appear intermittently (Wunsch, 1975), due perhaps to spatial and temporal variability of the stratified medium, but perhaps also to a fluctuating signal to noise level. However, data since acquired from the T/P altimeter have clearly demonstrated that energetic, phase-locked internal tides are indeed present in the open ocean and may propagate over thousands of kilometers before being dissipated. The best studied case is the internal tide generated along the Hawaiian Ridge. Using three years of T/P altimetric data, Ray and Mitchum (1996) showed that coherent propagation occurs from both sides of the ridge with an e-folding decay scale of about 1000 km. The net energy transfer rate from the barotropic to baroclinic tides along the ridge was estimated to be 15 GW, representing perhaps 7–8% of the 200 GW suggested by Munk (1997) as the global rate of baroclinic conversion for the M_2 tide. Kang *et al.* (2000) and Merrifield *et al.* (2001) have presented results from numerical models of internal tide generation at the Hawaiian Ridge.

The satellite altimetry has also indicated the existence of numerous additional generation regions for coherent baroclinic tides. Kantha and Tierney (1997) present a global survey using data smoothed over $2° \times 2°$ bins and show that phase-locked signals typically appear in the vicinity of undersea ridges. On the other hand, there are certain regions where large internal tides have been documented (e.g., southwest of the European shelf) that fail to show a significant signal in the T/P data. Ray and Mitchum (1997) suggest loss of temporal coherence with the barotropic tide as a plausible explanation.

Cherniawsky *et al.* (2001) recently discussed a technique for harmonic analysis of the T/P data using singular value decomposition (SVD) and applied the method to over 5 years (1992–97) of T/P altimetric data collected over the northeast Pacific. Their results permit identification of small-scale features and, in particular, they mention an internal tide signal apparently emanating from the Aleutian Island chain. Evidence for this was given in the residual amplitude and phase along T/P track 117. A localized source near the Aleutian Islands may also be discerned in the smoothed results of Kantha and Tierney (1997).

This paper further discusses the internal tide propagating south from the Aleutian Ridge into the central North Pacific using an updated analysis of the T/P data, combined with results of numerical simulations from barotropic and baroclinic models. Results from the T/P data show that the internal tide from the Aleutian Ridge appears as a directed beam of elevated amplitudes with a robust phase that can be traced for over 10° of latitude to the south. In the barotropic model, Amukta Pass is the dominant location for semi-diurnal tidal energy to cross the eastern half of the Aleutian Ridge and enter into the Bering Sea. The strongest cross-slope barotropic tidal volume fluxes along the eastern Aleutian Ridge occur in the vicinity of the Pass, providing the forcing for internal tides.

A high resolution, two-dimensional $(x-z)$ baroclinic model is applied to simulate the M_2 baroclinic tide generated at Amukta Pass. As expected, the model response includes an energetic internal tide propagating to the south away from the ridge topography. A comparison of the baroclinic component of the model sea-level response with along-track altimetric data shows that the phase of the sea-surface signature is well simulated both close to the source and in the far field. The results also demonstrate that the observed phase

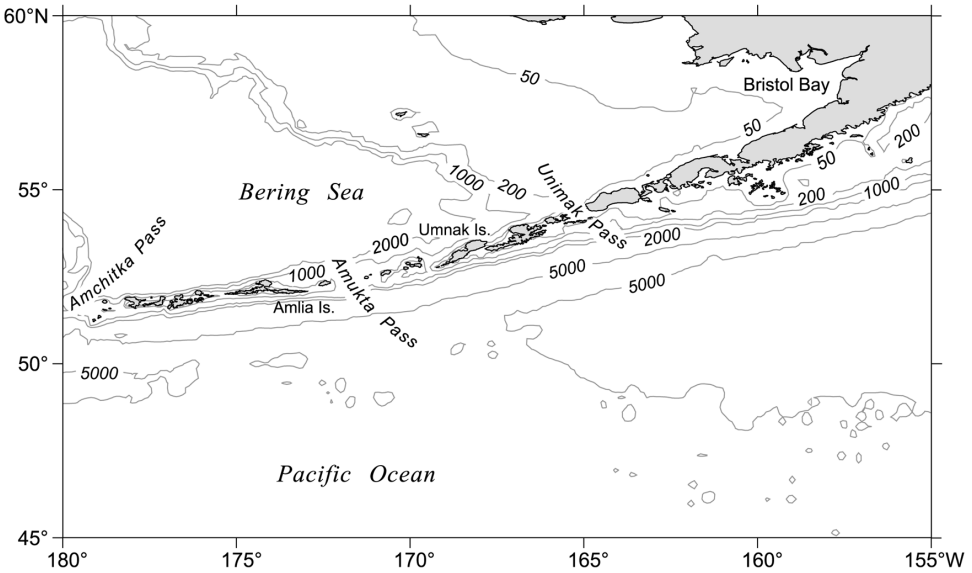

Figure 1. Map of the eastern Aleutian Island chain with place names and contours of bottom topography.

is significantly affected by the varying rotation rate encountered by the internal tide as it propagates southward into the central Pacific.

In the next section, the T/P altimeter observations of internal tides from the Aleutian Ridge are presented. Sections 3 and 4 discuss results of barotropic and baroclinic numerical models, respectively, including a comparison with the altimeter observations. The last section summarizes. For reference, an area map of the eastern Aleutian Island chain is included as Figure 1.

2. Observations from the T/P altimeter

The results presented here are derived from sea-level data obtained over the northeast Pacific Ocean by the T/P altimeter during cycles 1–250, representing nearly seven years of data from September, 1992 to July, 1999. Standard instrumental and geophysical corrections to the data, except for tidal analysis, were made at the Goddard Space Flight Center. Details on these algorithms may be found in Koblinsky *et al.* (1999). Tidal constants for 21 constituents were determined by a least-squares harmonic analysis method. This leads to an overdetermined matrix system which is solved using SVD (Cherniawsky *et al.,* 2001). The method also provides an estimate of the expected error, which scales with the standard deviation of the nontidal residual.

Since the T/P sampling rate of once every 9.9156 days is longer than the semidiurnal and diurnal periods, aliasing occurs between tidal constituents. A revised Rayleigh criterion (Parke *et al.,* 1987) gives the length of time series required to separate individual tidal

constituents. The time series of nearly 2500 days used in this study is easily of sufficient length to decouple M_2 (the only constituent considered below) from other tidal constituents. For example, separation of M_2 from S_2 requires about 1100 days of data. The principal source of aliasing error thus arises from broadband mesoscale eddies. Such variability is relatively weak over the central north Pacific, except perhaps immediately south of the Aleutian chain, where the Alaskan Stream, a swift (100 cm s^{-1}), narrow (50 km width), western boundary current is found. Even there mesoscale activity in the Stream is relatively weak in comparison to other western boundary currents like the Kuroshio or Gulf Stream (Reed *et al.,* 1991). A preprocessing of the data involving selective data trimming helps to reduce the projection of strong sea-level anomalies into the tidal signal. The estimated expected error for M_2 is about 1.8 cm in the vicinity of the Alaskan Stream, decreasing sharply to about 0.8 cm over most of the region of interest.

From results of the SVD analysis, a residual for M_2 is obtained by taking the difference between the observed harmonic and a smoothed version with high wavenumber variability removed. This procedure is fairly standard, but for completeness, a concise summary is given in the Appendix. The smoothed field, taken to represent the barotropic tide, is obtained from an eighth order polynomial fit to the alongtrack T/P data. The residual is interpreted as an internal tide signal plus background noise.

Figure 2 displays the amplitude of the resulting residual over the northeast Pacific. Except for a few distinct signals, amplitudes over most of the region are near a background level of 0.5–0.6 cm. This is the effective noise level and it appears to be somewhat lower than the formal estimate provided by the SVD analysis. Before turning our attention to the signal emanating from the Aleutian Ridge, we first note the other major sources of coherent internal tides over the region. The broad area of elevated amplitudes near the lower left side of Figure 2 is the far field expression of the internal tide originating from the northern flank of the Hawaiian Ridge (Ray and Mitchum, 1996). Also noteworthy are internal tide signals evident on either side of the Mendocino escarpment (125–130W, 30–43N), south of the Alaskan shelf (145–160W, 55–59N) and in the vicinity of the Queen Charlotte Islands off northern British Columbia (130–135W, 50–55N). Except for the latter, these signals could be discerned in the results of Kantha and Tierney (1997); the one occurring off the northern B.C. shelf may have been obscured by their spatial smoothing. However, the occurrence of a coherent internal tide in this region is consistent with the numerical modeling results of Cummins and Oey (1997) who obtained an energetic baroclinic tide radiating into the deep ocean from the shelf break to the north and south of the Queen Charlotte Islands. Directly west of these islands they showed a shadow zone, for which there is also evidence in the satellite data.

Figure 3 shows a close-up for the internal tide that apparently originates from the Aleutian Island chain in the vicinity of Amukta Pass. In addition to the amplitude field, the figure identifies (with an arrowhead symbol) the positions where the phase is 90° (deg UT) for regions where the amplitude is above the effective background noise level (0.6 cm). Phase increasing to the north or south is indicated by the

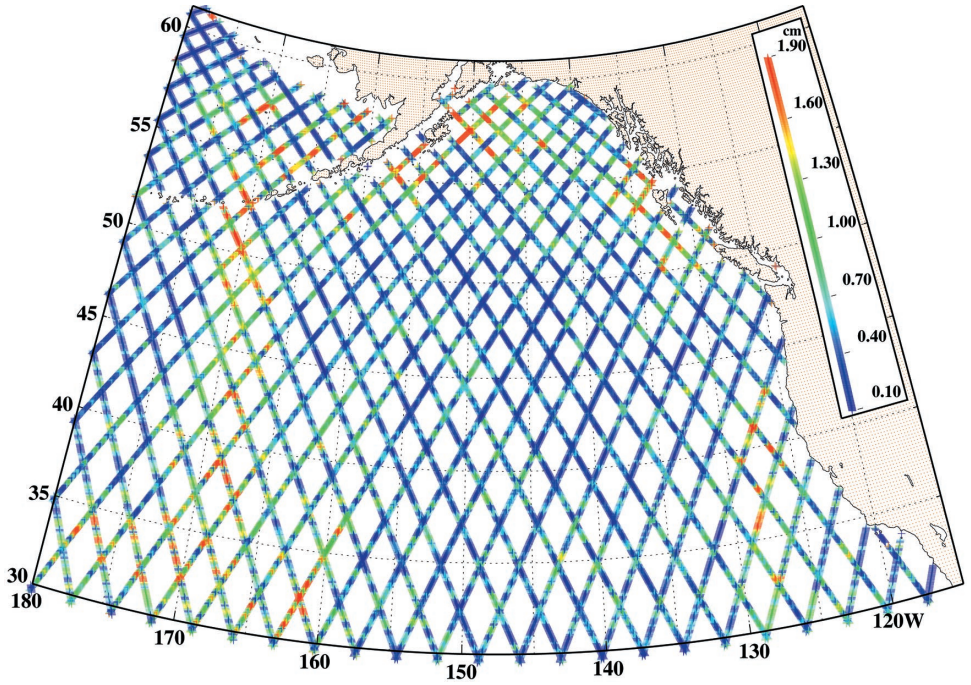

Figure 2. Plan view of the residual M_2 tidal amplitude after removal of the barotropic tide from the along-track T/P altimeter data. Residual amplitudes above background levels (≈0.6 cm) are identified as coherent internal tide signals.

direction of the arrowheads. In the North Pacific, the observations indicate coherent, directed propagation for a considerable distance (>1000 km) almost directly due south of the Aleutian Ridge into the central Pacific. The signal becomes difficult to distinguish south of 42N as it merges with the one originating from the Hawaiian Ridge. The data show relatively little geometrical spreading of the Aleutian Ridge internal tide, although such spreading could be obscured to some extent by a low signal to noise level off the main axis of the beam. Nevertheless the amplitude decay associated with geometrical spreading must not be significant, else the signal would attenuate rapidly down to the noise level. This suggests that the generating region along the ridge extends over a sufficiently large distance compared to a wavelength (nominally 150 km) so that it more closely resembles a line source, rather than a point source.

The phase signal shown in Figure 3 also shows propagation to the north of the ridge into the Bering Sea over a distance of about two wavelengths. Inspection of this northern signal shows that it is not as clearly defined as the one found to the south. Specifically, there is less regularity in the phase variation along T/P tracks, and, as well, less consistency between tracks crossing this signal. A possible reason that the

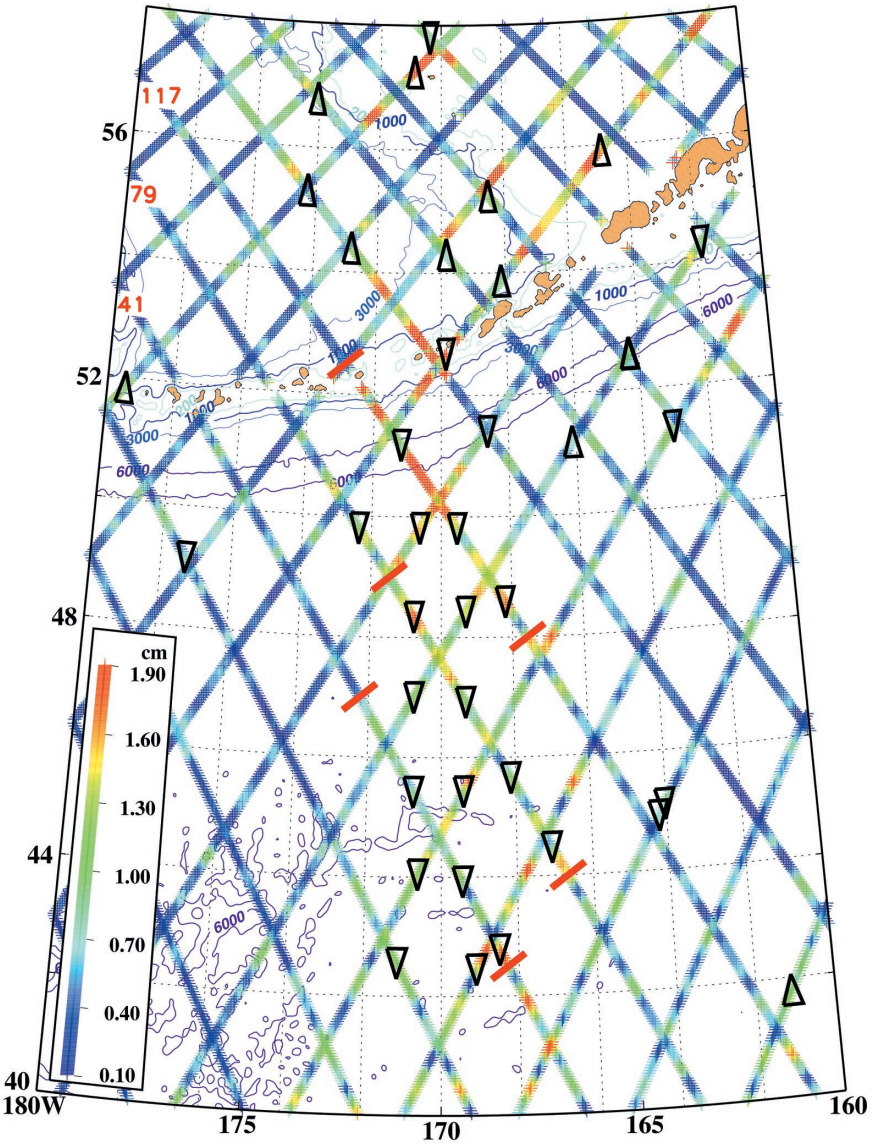

Figure 3. Plan view similar to Figure 2, but focusing on internal tides originating from the Aleutian Ridge near 170W. Locations of 90° phase (deg UT) for those regions where the amplitude of the residual is greater than 0.6 cm are indicated with the arrowhead symbol. The sense of the arrowhead indicates the direction of increasing phase. Bars placed across tracks 117, 79 and 41 indicate the portion of these tracks that are plotted in Figures 9 and 10.

northward signal is apparently more complicated than the one to the south may be the irregular, bowl-shaped topography found on the northern side of the ridge, with the presence nearby of the Bering Sea shelf. This could lead to multiple generation sites in this region, producing interfering signals and a complex structure. In spite of this uncertainty, the phase propagation evident in the T/P data does suggest that coherent internal tides in the eastern Bering Sea are predominantly generated along the northern flank of the Aleutian Ridge, rather than, for example, at the margin of the Bering Sea shelf.

3. Barotropic model

The next two sections discuss results from barotropic and baroclinic tidal models. The main purpose of using a barotropic model is to help explain why the region near Amukta Pass should be a site for generation of baroclinic tides and to estimate the forcing for a baroclinic model. The domain of the barotropic model includes the eastern part of the Aleutian Island chain and the southeastern Bering Sea. Barotropic tides in the Bering Sea have been described previously by Mofjeld (1986) and a recent review is available in Kowalik (1999). However, there has been little work done on tidal currents and energy fluxes through the passes in the Aleutian Island chain. Here we briefly describe results for the M_2 tide; a fuller discussion of barotropic model results will be presented elsewhere.

The spherical-coordinate, diagnostic, finite element model FUNDY5SP (Greenberg *et al.*, 1998) is used to compute tidal harmonics associated with sea-surface elevations and three-dimensional velocities over an area spanning the eastern Aleutian Islands and Bering Sea. Eight constituents (M_2, S_2, N_2, K_2, K_1, O_1, P_1, and Q_1) are included in iterative simulations with boundary conditions taken from the Egbert (1997) world tidal model. Tidal potential, earth tide, self-attraction and loading are applied as in Foreman *et al.* (2000). The model is pseudo-nonlinear through its inclusion of advection and an iterative approximation to quadratic bottom friction in the momentum equations. The numerical solution is obtained on a triangular grid with a resolution varying from 40 km over the deep ocean to 3 km nearshore and in the passages between the Aleutian Islands. Bathymetry for the model was taken from the ETOPO5, NOAA GEODAS, and Smith and Sandwell (1997) databases. No attempt has been made to represent the seasonal ice cover which occurs on the inner Bering Sea shelf.

An evaluation of the M_2 tide in the barotropic model was made by comparing the results with altimeter observations of the surface displacement at the crossover points of the T/P tracks. Based on modeled and observed harmonic constants, the rms difference over a tidal cycle, D, was computed as,

$$D = \left\{ \frac{1}{2} (A_m^2 + A_o^2) - A_m A_o \cos (\phi_m - \phi_o) \right\}^{1/2}. \tag{1}$$

Here A_o, A_m, ϕ_o, and ϕ_m denote the observed and modeled elevation amplitudes and phases, respectively. The error measure, D, was determined at the 93 crossover locations

distributed over the model domain where good rates of data return (>2/3 of the time) were obtained. Some points, located mostly over the northern Bering shelf, were not considered because of their poorer rates of data return, due presumably to the seasonal ice cover in the region. The average value of D at the 93 crossover points is 3.4 cm, while the average of the relative error (D/A_o) is 10.3%. The largest errors occur near Bristol Bay, probably reflecting a need for better local bathymetry and perhaps improvements in the parameterization of bottom friction. Overall, this comparison suggests that the model is reasonably accurate in its representation of the M_2 barotropic tide over the region.

A contour plot of the amplitude of the major semi-axis for the M_2 transport ellipses is shown in Figure 4a. The Aleutian Ridge generally presents an obstacle to cross-slope motions which are relatively weak along most of its length. However, in the vicinity of Amukta Pass, owing to the greater depth of this passage, the pattern is disrupted and significant cross-slope volume transports are obtained. The vertically-integrated barotropic energy flux vectors are given in Figure 4b. The predominant pattern in the Gulf of Alaska is a cyclonic gyre associated with propagation of a large-scale Kelvin wave around the basin. Significant leakage of tidal energy from the North Pacific into the eastern Bering Sea occurs in the region of the Amukta Pass. In particular, the model yields a total power crossing the ridge of 29 GW through Amukta Pass and the three other smaller passes found between Amlia and Umnak Islands. In contrast, relatively little M_2 tidal energy crosses Unimak Pass. (Locations are shown in Fig. 1.)

These results from the barotropic simulations indicate that for the eastern half of the Aleutian Ridge, the most pronounced cross-slope transport occurs in the vicinity of Amukta Pass. In two-dimensional models of internal tides (e.g., Baines, 1982; Morozov, 1995) the forcing is proportional to the the cross-slope volume flux, which is often the most important factor determining internal tide generation. On this basis, we may expect that the Amukta Pass region is the principal site along the eastern side of the Aleutian Ridge for the conversion of barotropic tidal energy into baroclinic tides. This corroborates the altimeter observations of Figure 3 which show an apparent internal tide signal emanating from this region. Significant cross-slope motions through Amukta Pass and other nearby passes are distributed along a 275 km portion of the ridge. Although the extent of the generation region is not particularly long compared to a wavelength of 150 km, it may be sufficient to account for the relative small degree of geometrical spreading evident in the observations.

4. Baroclinic model

A two-dimensional version of the sigma-coordinate Princeton Ocean Model (POM) is used to simulate internal tide generation at Amukta Pass and propagation into the North Pacific. The two-dimensional approach is useful because a large latitudinal range can be covered while maintaining good resolution in both horizontal and vertical coordinates. Representation of three-dimensional effects such as geometrical spreading is not attempted. Nevertheless, as shown below, the 2-D approach is able to capture the main

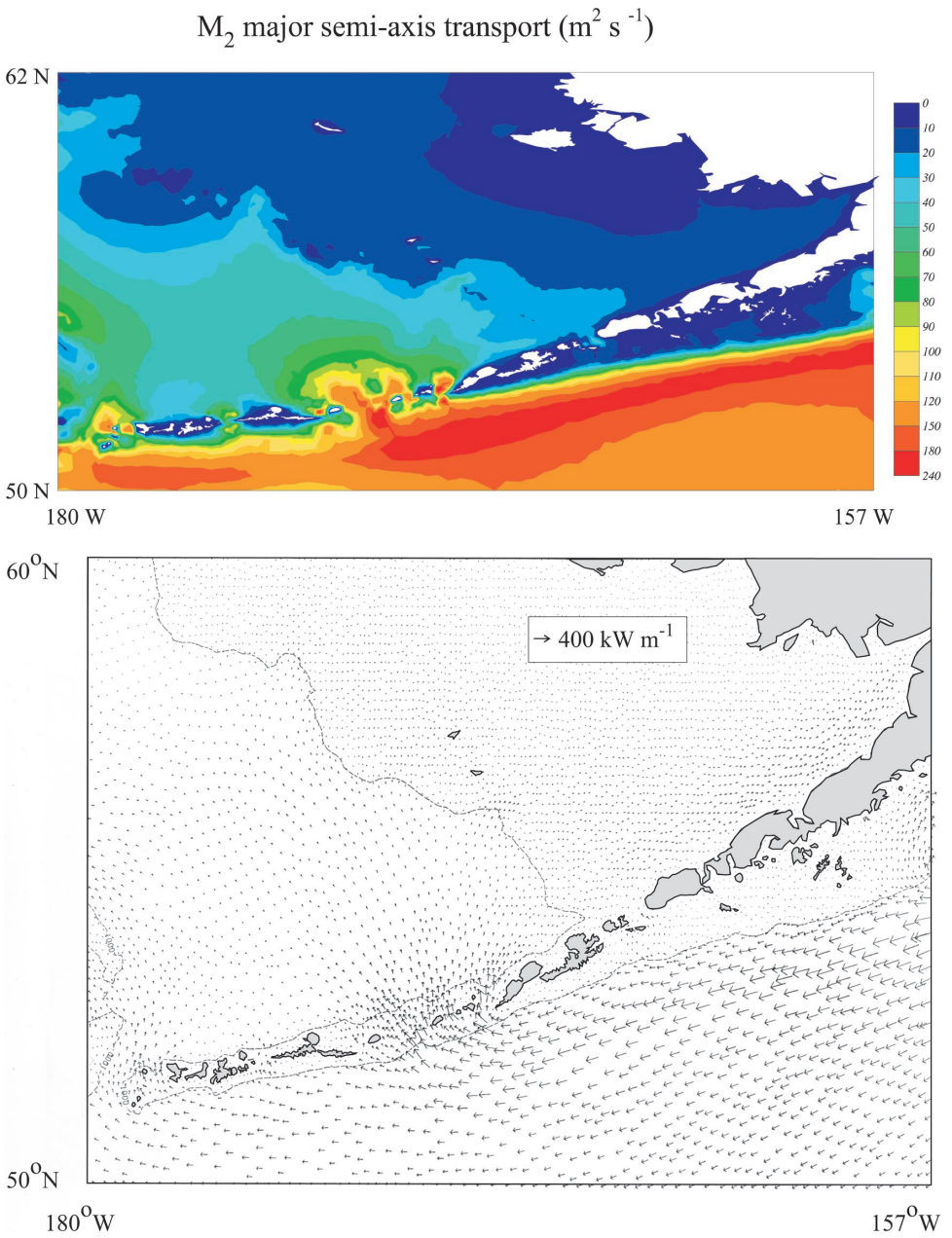

Figure 4. Results from the three-dimensional, finite element barotropic model. (a) Amplitude of the major semi-axis of the M_2 transport ellipses ($m^2\ s^{-1}$), and (b) depth-integrated barotropic energy flux for the M_2 constituent. The 1000 m bathymetric contour is indicated by the dashed line in (b).

features of propagation along the axis of the internal tidal beam, as observed in the T/P data.

Two topographic sections were considered, both crossing the Aleutian Ridge at Amukta Pass. One is aligned N-S along the 171.6W meridian; the second is inclined by about 12° counterclockwise with respect to north, so as to lie approximately normal to the Aleutian Ridge at the Pass. The results shown below are from the latter case; however, there was little to distinguish the model response with the two topographies. In particular the comparison with altimeter data was nearly unchanged. Topographic data are from the Smith and Sandwell (1997) bathymetry, smoothed with a 15 km wide boxcar filter. A uniform grid resolution of 1 km is specified over an inner region of variable topography spanning about 7° of latitude across the ridge. Depths are constant north and south of this inner region, and the grid resolution increases linearly to a maximum of 5 km at the boundaries. Since we are concerned only with the internal tide in the North Pacific, no attempt has been made to represent the shallow shelf bathymetry of the Bering Sea. There are 1201 grid points in the horizontal direction and 101 sigma levels in the vertical. These levels are distributed uniformly within the interior, but with enhanced resolution near the surface and the seabed. The model includes a realistic variation in the Coriolis parameter and comparison is made to a case with a uniform rotation rate.

The model is initialized with a horizontally homogeneous stratification approximating the annual mean density field of the North Pacific near the Aleutian Ridge. Figure 5 compares the initial vertical density profile and associated buoyancy frequency with those derived from the World Ocean Atlas climatology (Antonov *et al.*, 1998; Boyer *et al.*, 1998; henceforth WOA98) at 51.5N, 171.5W. Experiments were also conducted in which the initial stratification was modified to allow for a 100 m surface mixed layer, but the comparison with altimeter observations again showed little sensitivity to this change. The horizontally uniform stratification is only a first approximation, and a number of permanent features of the region (for example, the subpolar front) are not represented. Some justification for neglecting the influence of horizontal variations in the stratification on wave propagation is given at the end of Section 4b. The Alaskan Stream is also not included. The Stream is a sufficiently narrow current that the internal tide will propagate through it in a wave period or less, so that its influence is likely to be only local.

To complete the description of the model, we note that the model is driven on the southern open boundary through the north-south component of barotropic current oscillating at the M_2 frequency. Open boundary conditions are similar to those used by Oey and Chen (1992). In particular, a gravity wave radiation condition (Flather, 1976) is applied for the normal component of barotropic velocity and the surface elevation. The tangential component of the barotropic current at the boundaries is specified through a zero gradient condition. For the baroclinic velocity fields, an Orlanski radiation condition is applied, while a lateral advection condition is used to determine temperature and salinity at the boundaries (Oey and Chen, 1992). To facilitate long integrations, a ‘sponge’ layer is also implemented. Near the boundaries, temperature and salinity fields are relaxed back to

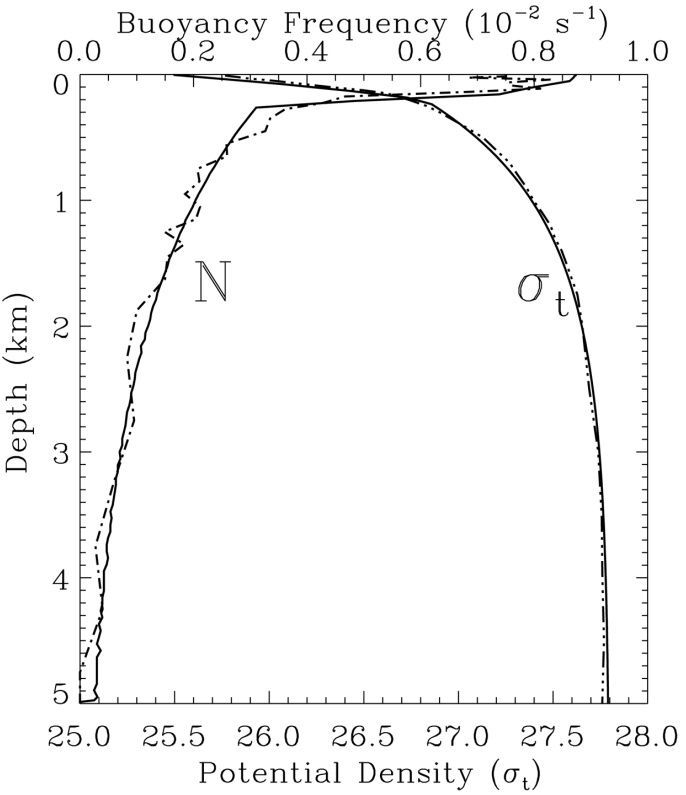

Figure 5. Comparison of the initial model profiles of potential density ($\sigma_t = \rho - 1000$) and buoyancy frequency, N, (solid lines) with observations (dashed lines) from the annual mean WOA98 climatology at 51.5N, 171.5W.

initial conditions on a time scale that varies from about 17 hours at a distance of 100 km to only 40 minutes directly at the boundary. This provides an absorbing region that effectively damps incident internal wave energy and also any reflected baroclinic motions due to inadequacies in the radiation conditions. The sponge layer has no effect on the barotropic mode.

Results discussed below are based on harmonic analyses of 24 hourly fields stored following a spin-up period of 20 days duration. Tests were conducted in which the spin-up period was varied between 8 and 80 days. While the comparison with the T/P data shows little sensitivity to these variations, some dependence is evident in the characteristics of the internal response. Specifically, appreciable differences were apparent in the depth-integrated baroclinic energy flux between 8-day and 20-day spin-up periods. This is presumably because sufficient time must be allowed for more slowly propagating higher modes to advance into the far field. A further extension to 40 and 80 days leads to only minor quantitative changes.

a. Results

Experiments were conducted in which the amplitude of the forcing at the southern open boundary was varied. A volume flux per unit length of 100 $m^2\ s^{-1}$ was found to yield a surface internal tide signal of comparable strength to the observed one. Most results presented below are from this basic case. By comparison, in the barotropic model the amplitude of the M_2 volume flux across the ridge near Amukta Pass is 19 Sv with about 60% occurring in the Amukta Pass itself and the rest through three smaller openings nearby. Averaging this flux over the approximately 200 km distance spanned by these openings yields a similar value of 95 $m^2\ s^{-1}$ for the laterally averaged flux.

Figures 6a and b present the amplitude and phase of the sea-surface displacement from the baroclinic model. There is a general progression of phase from south to north associated with propagation of the barotropic tide. Wiggles in the amplitude and phase are the surface expression of internal tides propagating away from either side of the ridge. Also shown are smooth curves, obtained from a polynomial fit to the model surface displacement (see Appendix A), which are taken to represent the barotropic tide.

The internal response of the model is characterized by the rms baroclinic current fields shown in Figure 7a, b. These fields were determined from a harmonic analysis of the horizontal velocity of the model. Also shown on the figure are the internal tide characteristics (rays) originating from 52.1N, a critical point where the magnitude of the bottom slope is equal to that of the rays. For hydrostatic waves ($N^2 \gg \omega^2$), the ray slopes are given by $dz/dx = \pm\sqrt{\omega^2 - f^2}/N$, where f is the Coriolis parameter, ω the angular frequency of the M_2 tide, and $N = \sqrt{-g\rho_0^{-1}d\rho/dz}$, the buoyancy frequency with ρ the potential density. As a critical slope is resonant for the baroclinic tide, this point is apparently the source for much of the variability found on the southern side of the ridge. The baroclinic current is most intense along this ray, which reflects off the bottom near 51.7N, and then off the surface at about 51N.

The ray structure gradually becomes incoherent and is lost south of about 49N. In the far field (Fig. 7b), the baroclinic current is intensified over the upper 500 m of the water column with maximum rms values of 10 to 12 cm s^{-1} occurring near the surface. The modal distribution of horizontal kinetic energy was determined by projecting the horizontal current onto the vertical modes (see Appendix B of Cummins and Oey, 1997). The results showed that beyond the immediate source region, the gravest internal mode dominates the baroclinic current. Accordingly, at 51N, the first mode accounts for half of the variance in the baroclinic current, increasing to 70–90% south of 46N.

A similar situation prevails on the northern side of the ridge (not shown) with an intense internal response occurring along the ray emanating downward from a critical point on the northern flank. Since the ridge is steeper on its northern side, the critical point is found at a shallower depth (370 m) than on the southern side. Away from the source, there is a comparable loss of the ray structure after a couple of reflections.

The depth-integrated baroclinic energy flux was determined from the harmonically analyzed fields (Cummins and Oey, 1997) and the results are shown in Figure 8. Jumps in

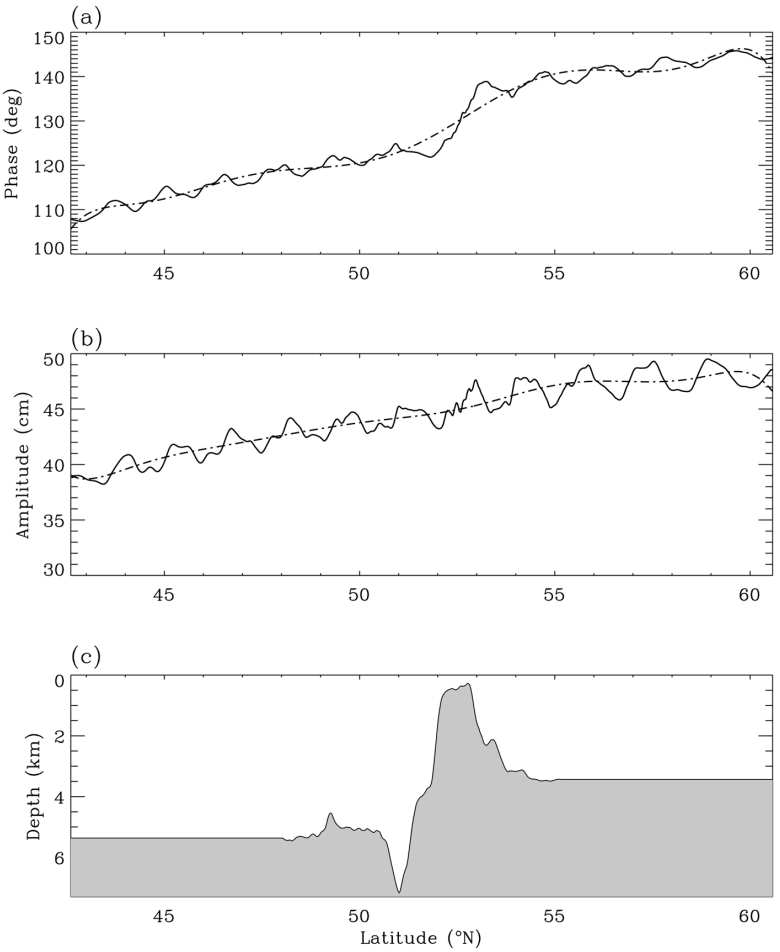

Figure 6. Solid lines give the phase (a) and amplitude (b) of the sea-surface displacement from the basic experiment with the baroclinic model. Phase and amplitude from an 8th order polynomial fit to the M_2 harmonic are also given (dashed lines). The lower panel (c) gives the bottom topography of the model.

the energy flux occur at the points on either side of the ridge crest where the bottom slope is critical. For the basic case (maximum volume flux of 100 $m^2\,s^{-1}$), the peak of the southwards energy flux is about 3000 W m^{-1}, decreasing to about 2000 W m^{-1} near 51N and then remaining almost constant. These values scale as the square of the cross-slope volume flux and are, therefore, sensitive to the magnitude of the barotropic forcing. A mean baroclinic conversion rate of 3000 W m^{-1} integrated over the approximately 200 km length of ridge with significant cross-slope barotropic forcing (Fig. 4a, b) implies a net baroclinic flux of about 0.6 GW into the N. Pacific.

The model response on the northern side of the ridge is associated with a baroclinic

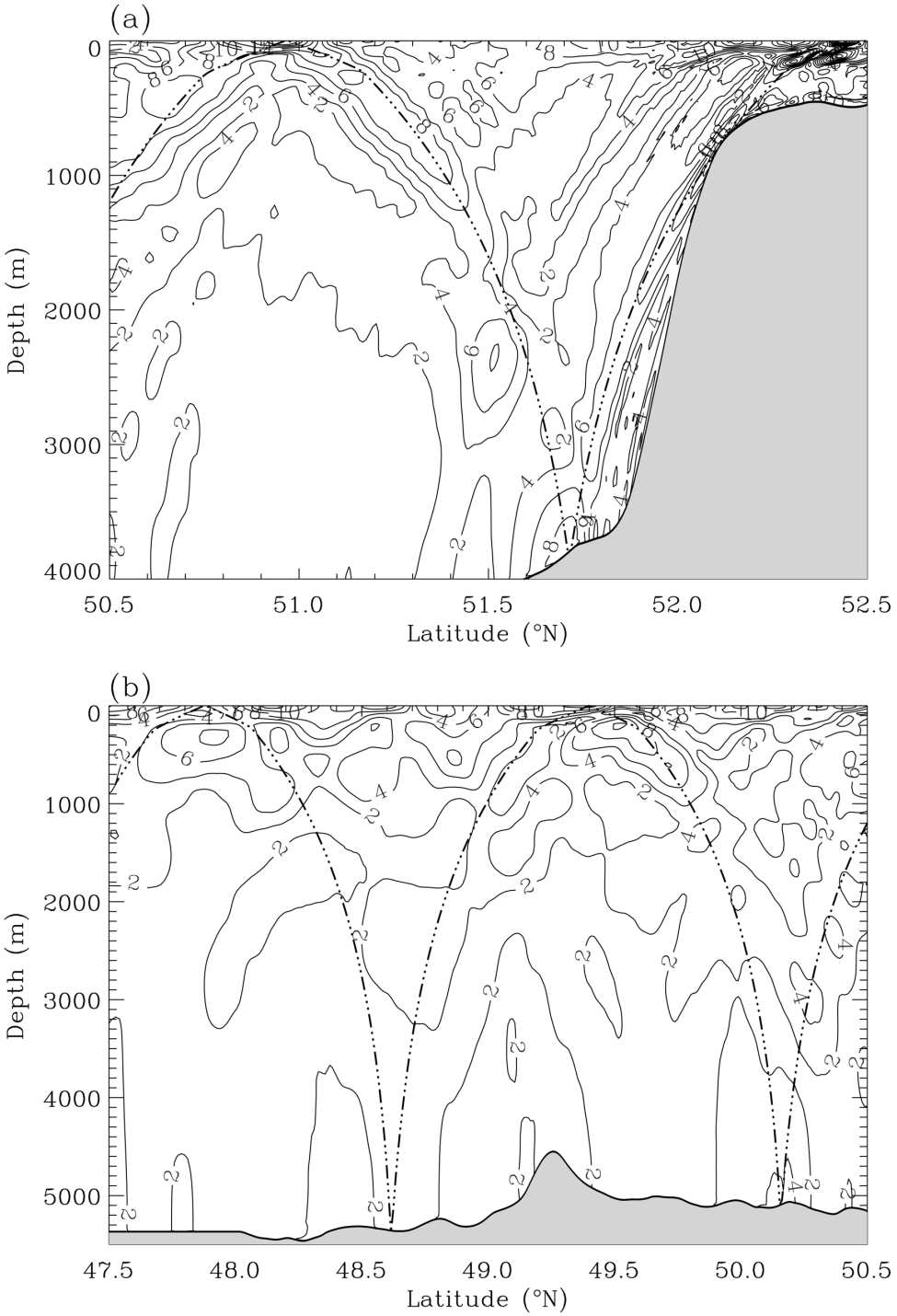

Figure 7. Rms M_2 baroclinic current on the southern flank of the ridge (a) and in the far field (b). The baroclinic velocity is computed as the residual horizontal velocity once the depth-averaged component is removed. Contours are drawn at 2 cm s^{-1} intervals from 2 to 20 cm s^{-1}. The dashed-dotted line indicates the path of a ray emanating from the critical point occurring at a depth of 740 m on the southern flank of the ridge.

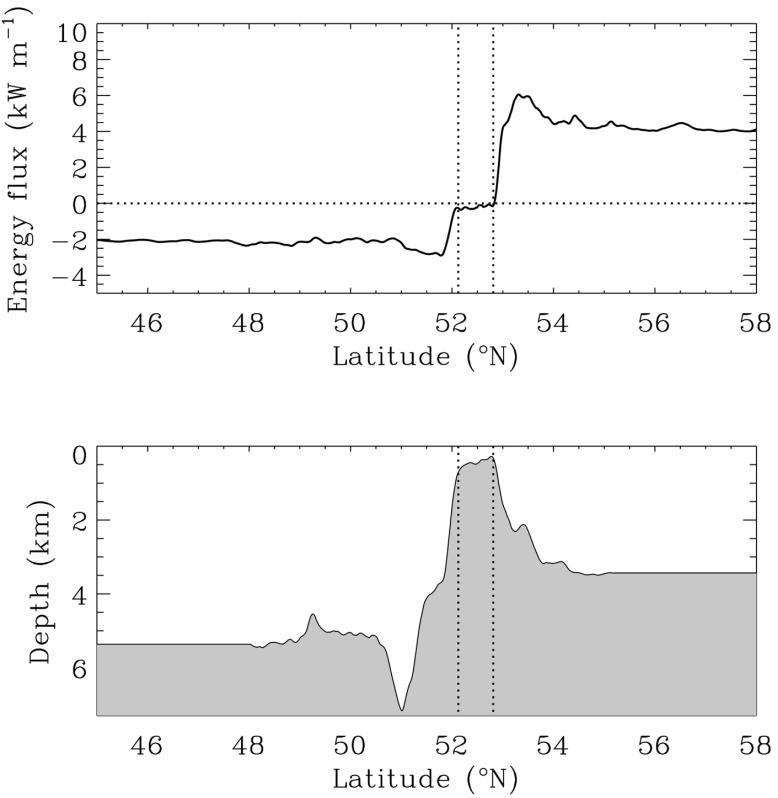

Figure 8. Depth-integrated baroclinic energy flux in W m^{-1} for the basic case. Negative values denote southward radiation of energy. The vertical dotted lines indicate the points near the ridge crest where the bottom slope is critical.

energy flux of about twice the magnitude of the one radiating southward. The strength of the forcing for internal tides is sensitive to the shape of the topography and the stratification near the generation region (Baines, 1982). The enhanced response to the north is due to the asymmetrical shape of the topography (steeper on the northern side) and the increased stratification near the shallower critical point. (By comparison, in a numerical experiment with an idealized symmetrical topography of comparable scale to the Aleutian Ridge, the model yielded similar energy fluxes on both sides of the ridge.)

Since the northern signal is less well defined in the altimetry data and the local three dimensionality of the topography likely more important, we are less confident that the model response is realistic to the north of the Ridge. If this component is nevertheless included, then the model yields an estimate of about 1.8 GW for the net baroclinic conversion near Amukta Pass. This value is 6% of the barotropic energy flux (Section 2) crossing the ridge in this region, and it represents about 1% of the global baroclinic conversion estimated by Munk (1997). Thus while the region near Amukta Pass is an

important source of coherent internal tides for the N. Pacific (e.g., Fig. 2), its significance in terms of global energy conversion is apparently quite limited.

b. Comparison with observations and evidence for refraction

Figure 9 presents a comparison between the sea-surface signature of the internal tide obtained from the model (black curves) and from the altimeter observations for three descending tracks in the North Pacific (T/P tracks 117, 79 and 41; colored curves). The top and middle panels of the figure show the latitudinal variation of phase, ϕ_i, and displacement amplitude, h_i, defined by Eqs. (A3) and (A4) of the Appendix, respectively. In the lower panel, the sea-surface displacement, at a fixed time ($t = 0$), $h_i \cos(\phi_i)$, is plotted against latitude. Each of the T/P tracks traverse the Aleutian Ridge internal tide obliquely over a range of latitudes. Accordingly, the data for each track are plotted over the latitudinal range in which the central region of the internal tide beam is traversed by the altimeter, with some overlap allowed between adjacent tracks. The portions of the three tracks plotted in Figure 9 are indicated in the plan view of Figure 3.

The upper panel of Figure 9 indicates that the phase of the internal tide in the model compares favorably with the observed phase. Although there are some discrepancies, these are relatively minor. In the far field, over nearly 10° of latitude (≈1100 km) from the source region, the model phase continues to agree with the observations. Phase from the overlapping tracks of data tends to be in mutual agreement, except perhaps in the vicinity of 48.5N and near 45N. At these respective latitudes, tracks 117 and 79 lie near the outer edge of the detectable beam of internal tidal energy and the small phase advance with respect to the center of the beam may be due to some geometrical spreading of the signal. The middle panel (Fig. 9b) indicates that the amplitude of the internal tidal signal from the model is comparable to that of the observations, especially in the far field. There is, however, little correspondence between model and observations with respect to fluctuations in the amplitude, h_i, which are generally below the noise level of the data. The largest discrepancies in amplitude occur close to the ridge. However, owing to the presence of the Alaskan Stream, this is also the region of largest measurement uncertainty. Overall, the model sea-surface displacement (Fig. 9c, lower panel) appears to be in generally good agreement with observations well into the far field.

The phase signal shown in Figure 9a is significantly affected by the variation in the Coriolis parameter. This is demonstrated straightforwardly by comparing the observed phase with that obtained from a numerical run in which the Coriolis parameter is given a constant value appropriate to 52N, the approximate latitude of the source region. The comparison is shown in Figure 10; for convenience the phase comparison from Figure 9a is reproduced in the figure. Close to the source, results are similar to the previous case. However, large systematic differences develop within 4°–5° south of the ridge between the observations and the model with uniform rotation rate, which fails to reproduce the observed phase signal. The variable rotation rate appears essential for accurate simulation of propagation into the far field.

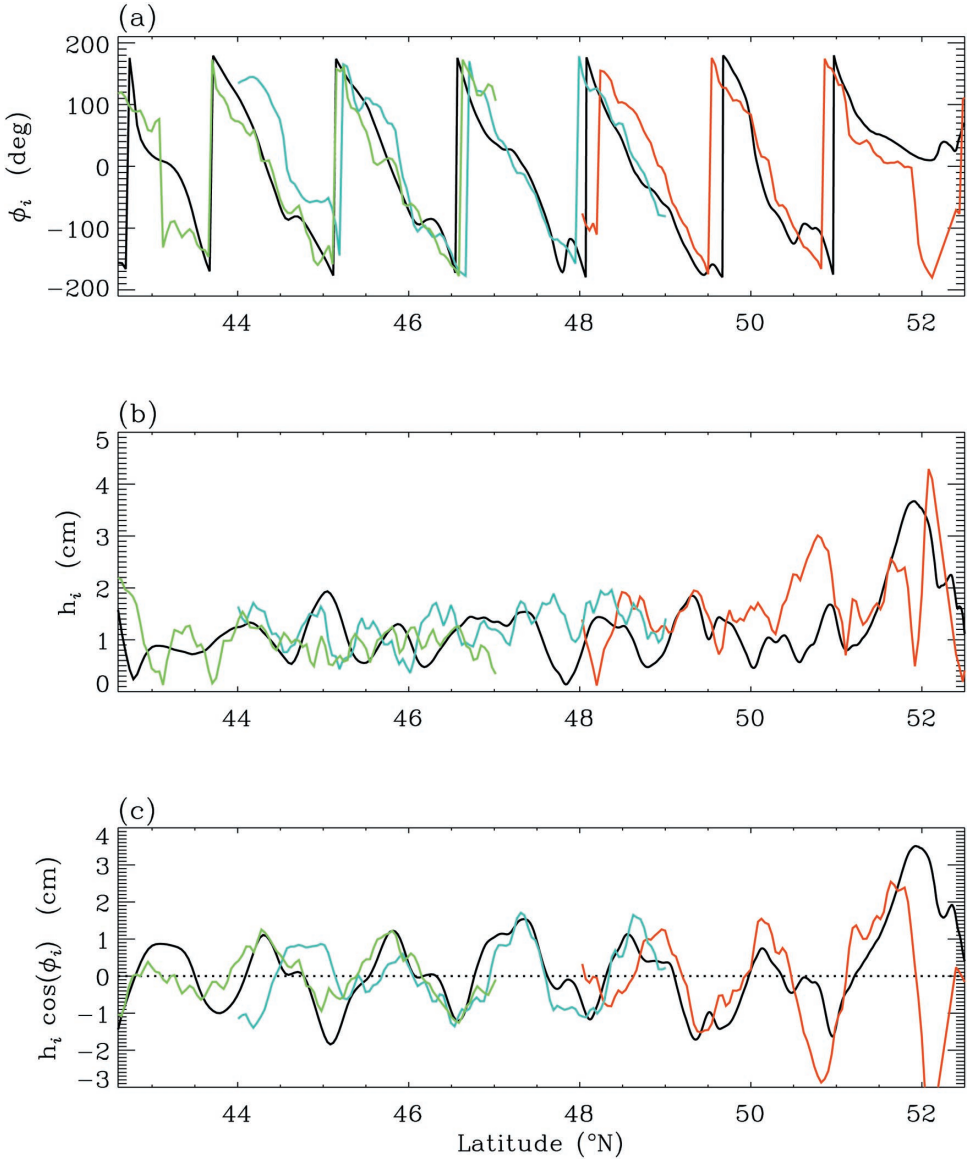

Figure 9. Comparison of the sea-surface signature of the internal tide from the model (black lines) with T/P data along tracks 117 (red lines), 79 (blue lines) and 41 (green lines). The plotted portions of these tracks are identified in Figure 3. The upper panel (a) shows the phase, ϕ_i, (deg UT) the middle panel (b) the amplitude, h_i, and the lower panel (c), the sea surface displacement at a fixed time ($t = 0$), $h_i \cos(\phi_i)$.

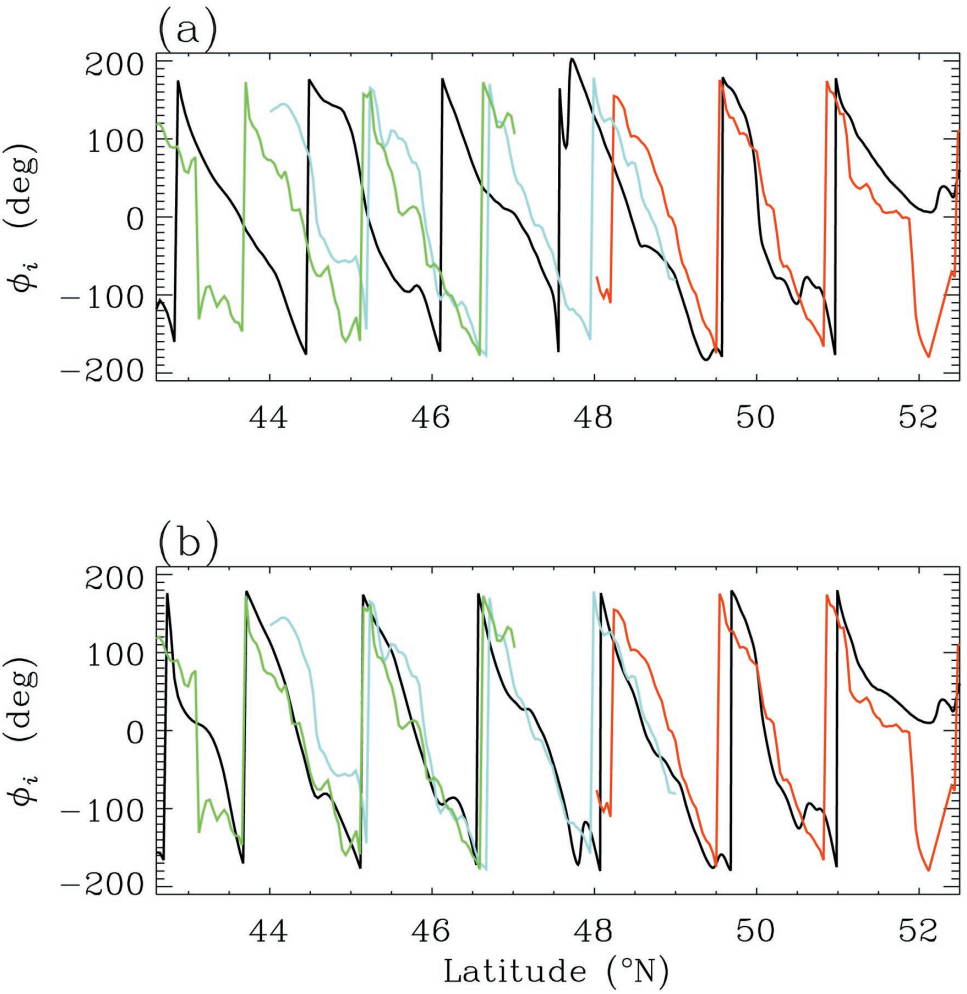

Figure 10. Comparison of the internal tidal phase from the model (black lines) with observed phases along T/P tracks (colored lines). The upper panel is from a numerical experiment with uniform rotation rate ($f = 2\Omega \sin 52°$), while the lower panel is with variable f (and identical to that in Fig. 9a).

The influence of a variable Coriolis parameter on phase may be understood in terms of a first mode plane wave whose local wavelength is gradually modulated as it propagates from north to south. As phase is the latitudinal integral of wavenumber, we have

$$\phi(\theta) = \phi(\theta_0) - \int_{\theta}^{\theta_0} kRd\theta', \tag{2}$$

where θ is a latitude coordinate, θ_0, the reference latitude of the source, k the wavenumber, and R, earth's radius. The wavenumber for vertical mode n is obtained from the local dispersion relation,

$$\omega^2 = c_n^2 k_n^2 + f^2, \tag{3}$$

where the Coriolis parameter $f = 2\Omega \sin\theta$, with Ω the angular velocity of the earth. The parameter, c_n, is the eigenvalue of the Sturm Liouville equation governing the vertical modes, $\Pi_n(z)$, for hydrostatic internal waves (LeBlond and Mysak, 1978),

$$\frac{d}{dz}\left(\frac{1}{N^2}\frac{d\Pi_n}{dz}\right) + \frac{\Pi_n}{c_n^2} = 0, \tag{4}$$

with boundary conditions, $d\Pi_n/dz = 0$ at $z = 0, -H$.

Taking the negative root in (3) for southward propagation ($k_n < 0$) and substituting into (2) we have

$$\phi(\theta) = \phi(\theta_0) + \omega \int_{\theta}^{\theta_0} \sqrt{\frac{1 - \gamma^2 \sin^2\theta'}{c_n^2}}\, R d\theta', \tag{5}$$

where $\gamma = 2\Omega/\omega$. If c_n is assumed independent of latitude, (5) has an exact integral (Gradshteyn and Ryzhik, 2000; p. 198) given by

$$\phi(\theta) = \phi(\theta_0) + \frac{R\omega}{c_n}\,(I(\theta_0) - I(\theta)), \tag{6}$$

where

$$I(\theta) = \int \sqrt{1 - \gamma^2 \sin^2\theta}\, d\theta = \gamma E(\alpha, \gamma^{-1}) - \frac{(\gamma^2 - 1)}{\gamma} F(\alpha, \gamma^{-1}) \quad [\gamma^2 > 1],$$

$\alpha = \arcsin(\gamma \sin\theta)$ and

$$F(\alpha, p) = \int_0^{\alpha} \frac{d\xi}{\sqrt{1 - p^2 \sin^2\xi}} \quad [p^2 < 1],$$

$$E(\alpha, p) = \int_0^{\alpha} \sqrt{1 - p^2 \sin^2\xi}\, d\xi \quad [p^2 < 1]$$

are elliptic integrals of the first and second kind, respectively.

Setting $\phi(\theta_0)$ arbitrarily to zero and taking $\theta_0 = 52$N, $\phi(\theta)$ was determined from (6) with the algorithm given in Press *et al.* (1992) used to compute the elliptic integrals. The buoyancy frequency, $N(z)$, was based on the mean annual stratification from the WOA98 climatology at 51.5N, 171.5W. Eq. (4) then yields $c_1 = 2.08\ \mathrm{m\ s^{-1}}$ for the dominant gravest internal mode.

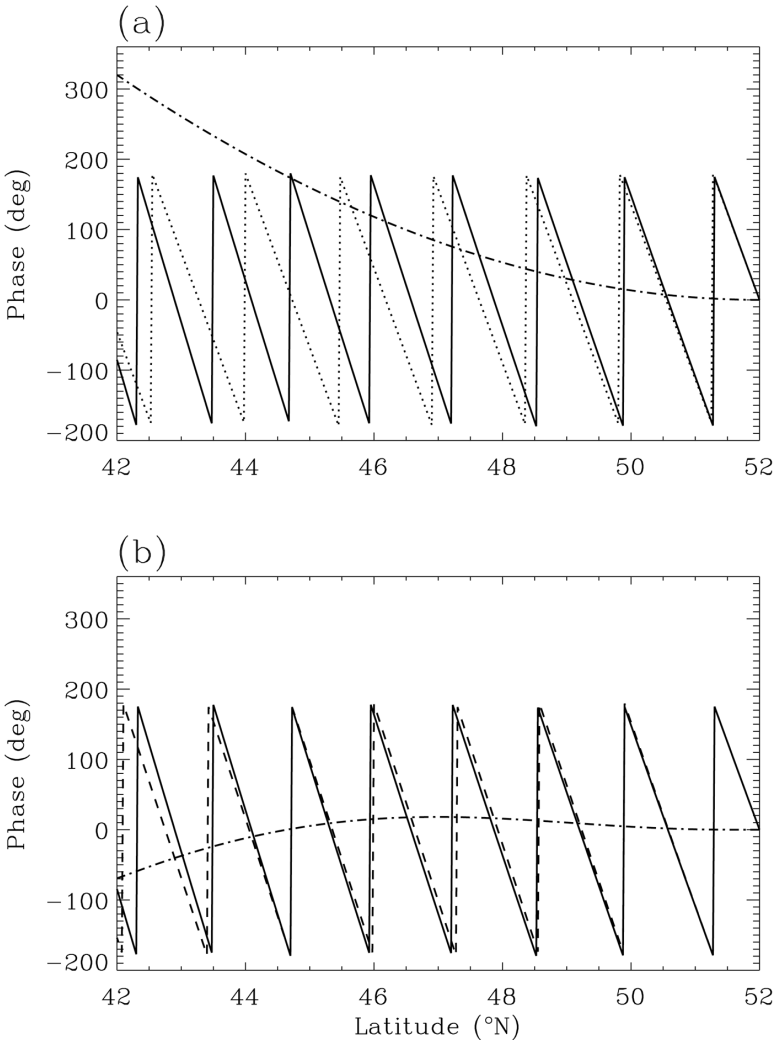

Figure 11. (a) Comparison of phase, $\phi(\theta)$, given by Eq. (6) (solid line) to a case with constant Coriolis parameter (dotted line). The eigenvalue, c_1, is constant for both cases. (b) The solid line repeats the solution of (6) given in (a), while the dashed line is a numerical solution of (5) with c_1 now dependent on latitude. The dash-dotted line in (a) and (b) gives the cumulative phase difference from the source between the respective cases.

Figure 11a compares the phase from (6) with a case in which the phase varies linearly with the Coriolis parameter held constant at the value appropriate to 52N. The two cases gradually diverge away from the source with the phase difference becoming appreciable over a few degrees of latitude, much as in Figure 10a. The cumulative phase difference over 10° of latitude is 320°. Thus, the slow variation in the Coriolis parameter encountered

by the internal tide as it propagates to the south may be expected to lead to a progressive decrease in wavelength, significantly affecting the phase of the signal. This is essentially a refraction phenomena and it largely accounts for the results of Figure 10, where the cumulative phase difference at the southern boundary between the two numerical experiments is about 300°. In the altimeter observations, small variations in wavelength are difficult to discern. However, the integrated effect on the phase appears to be readily detectable.

As a check on the influence of horizontal variations in stratification, $\phi(\theta)$ was recalculated from (5) with latitudinal variations in c_1 retained. Data from the WOA98 climatology were used to compute c_1 along 171.5W, from 51.5N to 42.5N at 1° intervals. These values were linearly interpolated onto a fine resolution grid and (5) was integrated numerically. The results are given in Figure 11b and compared to the previous case with constant c_1. For most of the latitude range, $\phi(\theta)$ is nearly indistinguishable between the two cases. Only toward the southern end of the region do variations in stratification begin to have a noticeable, yet still comparatively small, influence on the phase. For the latitude range considered, Coriolis parameter variations appear to have considerably greater influence on refraction of the internal tide from Aleutian Ridge than lateral inhomogeneities in the stratification. This provides some justification for the initial horizontally homogeneous stratification of the model.

c. Vertical mixing

Aside from the intrinsic interest that such a phenomena may hold, internal tides are potentially important because they may make a significant contribution to vertical mixing processes in the ocean. The numerical model suggests that baroclinic energy conversion on the southern flank of the ridge occurs at a rate of about 3000 W m^{-1}. Following arguments given by Munk and Wunsch (1998, §3.3), an internal tide carrying an energy flux of this magnitude with *e*-folding dissipation scale of $O(1000$ km) will lead to a vertical diffusivity within the interior of $O(10^{-5}\ m^2\ s^{-1})$. This value corresponds to the 'pelagic' diffusivity of Munk and Wunsch (1998) and is consistent with observations taken over much of the ocean interior (e.g., Kunze and Sanford, 1996). However, it is usually considered insufficient to maintain the abyssal stratification of the ocean.

Except for the bottom logarithmic layer, the vertical diffusivity over almost the entire model domain is dominated by the weak background constant ($2 \times 10^{-5}\ m^2\ s^{-1}$) that is added to the mixing coefficient determined from the level—2.5 turbulence closure scheme of Mellor and Yamada (1982). However, the internal tide produces strong shears near the generation region and the turbulence closure responds with large mixing coefficients in localized areas. Figure 12 shows the mean vertical diffusivity produced by the closure scheme near the crest of the ridge. Large mixing coefficients ($>10^{-2}\ m^2\ s^{-1}$) occur within the interior in localized patches on either side of the ridge crest. The turbulent kinetic energy field (not shown) has a similar pattern. Superposed on the figures are the internal tide characteristics emanating from the two points nearest the crest where the bottom slope

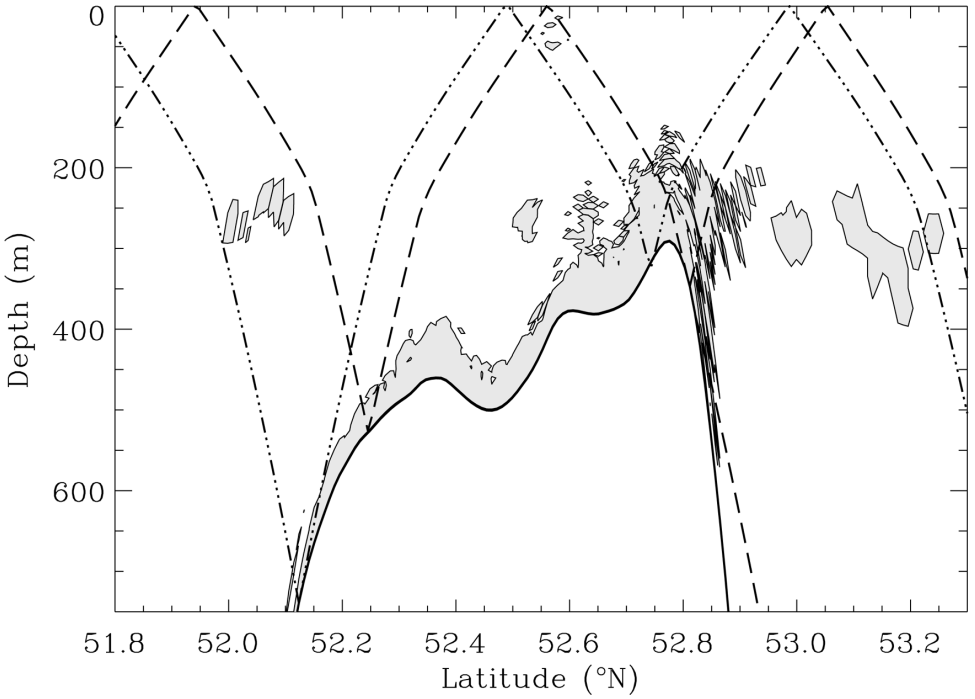

Figure 12. Time-averaged vertical diffusivity near the crest of the ridge from the basic experiment. The filled contour delineates regions where the diffusivity is greater than 10^{-2} m^2 s^{-1}. The broken lines indicate ray paths emanating from critical points on either side of the ridge.

is critical (cf. Fig. 7). Although the regions of large turbulent kinetic energy and mixing are rather irregularly distributed, they appear to be associated with the internal tide characteristics. Strong shears between regions of intense internal tidal motions along these ray paths and adjacent quiescent regions apparently produce the patches of turbulent mixing in the model.

There are, of course, no measurements to verify this aspect of the model response. Nevertheless, these results bear a qualitative similarity to the recent dissipation measurements of Gregg *et al.* (1999) taken over a submarine fan on the north side of Monterey Bay. They showed intense turbulence and mixing in a 50 m wide beam extending 5–6 km offshore and lying along an internal tide characteristic. Figure 12 suggests that the Mellor-Yamada parameterization is able to capture aspects of intense turbulent mixing associated with the tidal rays, and that this may be a general feature of the near-field response.

5. Summary

Satellite altimeter measurements have demonstrated the existence of coherent internal tides in the ocean whose phase propagation may be traced over large distances. The global

survey of Kantha and Tierney (1997) shows that these signals occur throughout the world ocean and originate principally from large submerged ridge topography. This paper has considered the North Pacific internal tide signal originating from the Aleutian Ridge. In this case, over most of the length the ridge, the large topography and associated complex of islands block the cross-slope barotropic motions required to generate internal tides. However, as demonstrated in simulations with a barotropic tidal model, strong cross-slope motions do occur in and around Amukta Pass, a relatively deep gap in the ridge. This permits the generation of a directed, coherent internal tide that propagates into the central North Pacific. There is also a similar but less clearly defined signal which propagates to the north into the southern Bering Sea.

A high resolution, two-dimensional version of the Princeton Ocean Model was applied to examine generation and propagation of the M_2 internal tide emanating from Amukta Pass. Comparison with the T/P observations shows that the model is able to capture the surface signature of the internal tide as it propagates over 1100 km southward into the central North Pacific. The phase of this signal is the most robust aspect of the observations and the comparison shows that it is sensitive to the latitudinal variation of the Coriolis parameter. This sensitivity is consistent with an expected phase modulation due to gradual reduction in the wavelength of a first mode internal plane wave propagating to the south.

Over almost the entire model domain, the vertical mixing coefficient is dominated by the weak background constant that supplements the parameterization of turbulence in the model. There are, however, isolated interior regions close to the ridge crest where strong shears obtain, and the turbulence closure scheme yields large mixing coefficients. These regions occur near the internal tide characteristics emanating from locations where the bottom slope is critical. This result appears to be qualitatively consistent with recent observations by Gregg *et al.* (1999) of intense turbulent dissipation along an internal tide ray.

The numerical model yields a net baroclinic energy conversion rate near Amukta Pass of about 9000 W m^{-1}, with one third of this total radiating southward into the central North Pacific. Assuming that this is the average rate of baroclinic energy production along the 200 km region of cross-slope barotropic flow implies an integrated baroclinic flux of about 1.8 GW. In global terms this represents perhaps 1% of the total baroclinic energy conversion for the M_2 tide.

An improved estimate of baroclinic conversion at the Aleutian Ridge will likely require application of a three-dimensional baroclinic model. Such a model would permit an assessment of the influence of smaller scale transverse topographic irregularities along the ridge in scattering additional barotropic energy into baroclinic motions. Further problems that could be addressed with a three-dimensional model include an assessment of the influence of the Alaskan Stream, information on propagation and dissipation of internal tides in the Bering Sea, and a determination of the extent of geometrical spreading of the southward radiating signal.

APPENDIX

Separating the surface signature of the internal tide

We assume that tidal oscillations of sea surface, η_o, are the sum of contributions from surface, η_s, and internal, η_i tides,

$$\eta_o = \eta_s + \eta_i. \tag{A1}$$

Expressed in harmonic form we have

$$\eta_i = h_i \cos(\omega t - \phi_i) = a_i \cos(\omega t) + b_i \sin(\omega t), \tag{A2}$$

where ω is the M_2 frequency and $(a_i, b_i) = (h_i \cos(\phi_i), h_i \sin(\phi_i))$. Similar forms are assumed for η_o and η_s. The internal tidal phase, ϕ_i, and amplitude, h_i, are then given by

$$\phi_i = \tan^{-1}(B/A), \tag{A3}$$

$$h_i = A/\cos(\phi_i), \tag{A4}$$

where $(A, B) = (a_o - a_s, b_o - b_s)$. The barotropic tidal component, (a_s, b_s), is determined from a least-squares polynomial fit to (a_o, b_o). The order of this polynomial was chosen so as to provide a smoothing length scale of about 300 km. The results shown are based on an 8th order polynomial fit to the T/P data. The model sea surface was treated similarly, and it was verified that results are essentially unchanged using a 6th order fit.

REFERENCES

Antonov, J.I., S. Levitus, T.P. Boyer, M.E. Conkright, T. O'Brien and C. Stephens. 1998. World Ocean Atlas 1998 Vol. 2: Temperature of the Pacific Ocean. NOAA Atlas NESDIS 28, U.S. Government Printing Office, Washington, DC.

Baines, P.G. 1982. On internal tide generation models. Deep-Sea Res., *29,* 307–338.

Boyer, T.P., S. Levitus, J.I. Antonov, M.E. Conkright, T. O'Brien and C. Stephens. 1998. World Ocean Atlas 1998 Vol. 5: Salinity of the Pacific Ocean. NOAA Atlas NESDIS 30, U.S. Government Printing Office, Washington, DC.

Cherniawsky, J.Y., M.G.G. Foreman, W.R. Crawford and R.F. Henry. 2001. Ocean tides from TOPEX/POSEIDON sea level data. J. Atmos. Ocean. Tech., *18(4),* 649–664.

Cummins, P.F. and L.Y. Oey. 1997. Simulation of barotropic and baroclinic tides off northern British Columbia. J. Phys. Oceanogr., *27,* 762–781.

Egbert, G.D. 1997. Tidal data inversion: interpolation and inference. Progr. Oceanogr., *40,* 53–80.

Flather, R.A. 1976. A tidal model of the northwest European continental shelf. Mem. Soc. R. Sci. Liege, Ser. 6, *10,* 141–164.

Foreman, M.G.G., W.R. Crawford, J.Y. Cherniawsky, R.F. Henry and M.R. Tarbotton. 2000. A high-resolution assimilating tidal model for the Northeast Pacific Ocean. J. Geophys. Res., *105,* 28629–28651.

Gradshteyn, I.S. and I.M. Ryzhik. 2000. Table of Integrals, Series, and Products, 6th ed., A. Jeffrey and D. Zwillinger, eds., Academic Press, 1163 pp.

Greenberg, D.A., F.E. Werner and D.R. Lynch. 1998. A diagnostic finite element ocean circulation model in spherical-polar coordinates. J. Atmos. Ocean. Tech., *15,* 942–958.

Gregg, M.C., D.W. Winkel, J.A. Mackinnon and R.C. Lien. 1999. Mixing over shelves and slopes, *in*

Dynamics of Oceanic Internal Gravity Waves, II. Proceedings 'Aha Huliko'a, Hawaiian Winter Workshop, University of Hawaii at Manoa, January 18–22, 1999.

Kang, S.K., M.G.G. Foreman, W.R. Crawford and J.Y. Cherniawsky. 2000. Numerical modelling of internal tide generation along the Hawaiian Ridge. J. Phys. Oceanogr., *30,* 1083–1098.

Kantha, L.H. and C.G. Tierney. 1997. Global baroclinic tides. Progr. Oceanogr., *40,* 163–178.

Koblinsky, C.J., R. Ray, B.D. Beckley, Y.-M. Wang, L Tsaoussi, A. Brenner and R. Williamson. 1999. NASA Ocean Altimeter Pathfinder Project, Report 1: Data Processing Handbook. Technical Memorandum NASA/TM-1998-208605, 55 pp.

Kowalik, Z. 1999. Bering Sea Tides, *in* The Bering Sea: Physical, Chemical and Biological Dynamics, T. Loughlin and K. Ohtani, eds., Alaska Sea Grant Press, Fairbanks, AK, 93–127.

Kunze, E. and T.B. Sanford. 1996. Abyssal mixing: where it isn't. J Phys. Oceanogr., *26,* 2286–2296.

LeBlond, P.H. and L.A. Mysak. 1978. Waves in the Ocean, Elsevier, 602 pp.

Mellor, G.L. and T. Yamada. 1982. Development of a turbulent closure model for geophysical fluid problems. Rev. Geophys. Space Phys., *20,* 851–875.

Merrifield, M.A., P.E. Holloway and T.M. Shaun Johnston. 2001. The generation of internal tides at the Hawaiian Ridge. Geophys. Res. Lett., *28,* 559–562.

Mofjeld, H.O. 1986. Observed tides on the northeastern Bering Sea shelf. J. Geophys. Res., *91,* 2593–2606.

Morozov, E.G. 1995. Semidiurnal internal wave global field. Deep-Sea Res., *42,* 135–148.

Munk, W.H. 1997. Once again—once again—tidal friction. Progr. Oceanogr., *40,* 7–35.

Munk, W.H. and C. Wunsch. 1998. Abyssal recipes II: energetics of tidal and wind mixing. Deep-Sea Res. I, *45,* 1978–2010.

Oey, L.Y. and P. Chen. 1992. A model simulation of circulation in the northeast Atlantic shelves and seas. J. Geophys. Res., *97,* 20087–20115.

Parke, M.E., R.H. Stewart, D.L. Farless and D.E. Cartwright. 1987. On the choice of orbits for an altimetric satellite to study ocean circulation and tides. J. Geophys. Res., *92,* 11693–11707.

Press, W.H., S.A. Teukolsky, W.T. Vettering and B.P. Flannery. 1992. Numerical Recipes in Fortran, 2nd ed., Cambridge University Press, New York, NY, 963 pp.

Ray, R.D. and G.T. Mitchum. 1996. Surface manifestation of internal tides generated near Hawaii. Geophys. Res. Lett., *23,* 2101–2104.

____1997. Surface manifestation of internal tides in the deep ocean: observations from altimetry and island gauges. Progr. Oceanogr., *40,* 135–162.

Reed, R.K., F.I. Gonzalez and L. Miller. 1991. On the structure and stability of the Alaskan Stream. J. Mar. Res., *49,* 719–726.

Smith, W.H.F. and D.T. Sandwell. 1997. Global sea floor topography from satellite altimetry and ship depth soundings. Science, *277,* 1956–1962.

Wunsch, C. 1975. Internal tides in the ocean. Rev. Geophys. and Space Phys., *13,* 167–182.

Received: *5 October, 2000;* revised: *20 February, 2001.*